



UKAEA-CCFE-PR(25)349

R. Kerr, M. Gilbert, S. Murphy

Relating the formation energies for oxygen vacancy defects to the structural properties of tungsten oxides

Enquiries about copyright and reproduction should in the first instance be addressed to the UKAEA Publications Officer, Culham Science Centre, Building K1/0/83 Abingdon, Oxfordshire, OX14 3DB, UK. The United Kingdom Atomic Energy Authority is the copyright holder.
The contents of this document and all other UKAEA Preprints, Reports and Conference Papers are available to view online free at scientific-publications.ukaea.uk/

Relating the formation energies for oxygen vacancy defects to the structural properties of tungsten oxides

R. Kerr, M. Gilbert, S. Murphy

Computational Materials Science

Relating the formation energies for oxygen vacancy defects to the structural properties of tungsten oxides --Manuscript Draft--

Manuscript Number:	COMMAT-D-24-02584
Article Type:	Full Length Article
Section/Category:	Atomic Description
Keywords:	tungsten; WO3; DFT; oxygen vacancy
Corresponding Author:	Samuel Murphy Lancaster University Lancaster, UNITED KINGDOM
First Author:	Ryan Kerr
Order of Authors:	Ryan Kerr
	Mark Gilbert
	Samuel Murphy
Abstract:	Tungsten is one of the primary materials of choice for several commercial fusion power plant designs, in particular for divertor targets and the first wall. In maintenance conditions or during a loss of coolant accident, tungsten is expected to reach temperatures at which it readily volatilises as tungsten trioxide, potentially distributing radioactive material and posing a hazard to personnel. The oxidation of tungsten is reported to show an orientation dependence, however, the mechanism by which it occurs is not fully understood on an atomic level, providing a barrier to the understanding of tungsten smart alloys, which are being developed to reduce oxidation and mitigate the hazards. From the DFT+U simulations, we show how key features of the electronic structure of the tungsten-oxygen system change as the tungsten-oxygen ratio evolves. We then calculate the formation energies of oxygen vacancies and migration barriers for their diffusion, allowing an assessment of their mobility in the different tungsten oxide phases. Our results provide a new level of understanding of the sub-stoichiometric Magneli phases that are observed during the oxidation of tungsten, which are perceived to be composed of WO2 - and WO 3 -like regions.
Suggested Reviewers:	Christopher Race christopher.race@sheffield.ac.uk Simon Phillpot sphil@mse.ufl.edu
	Rob Jackson r.a.jackson@keele.ac.uk



Samuel Murphy,

School of Engineering,

Lancaster University,

Bailrigg,

Lancaster,

LA1 4YW

11th September 2024

Dear Editor,

On behalf of my co-authors and I, I would like to submit our manuscript titled "Relating the formation energies for oxygen vacancy defects to the structural properties of tungsten oxides" for publication in Computational Materials Science as a regular article. In this manuscript we use Density Functional Theory (DFT) to explore how structural motifs in tungsten oxide phases affect the stability and mobility of oxygen vacancy defects and use this information to comment on the implications for the oxidation of tungsten, which is a potential issue in the event of an accident at a future fusion powerstation. Our results show that the formation energies for the oxygen vacancy defects in WO_3 are lower than in WO_2 and therefore, regions of the Magneli phases that structurally resemble the trioxide have lower defect formation energies than those that are similar to WO_2 . This introduces an anisotropy into the diffusivity of oxygen through the material and ,as a consequence, the orientation of the growth of the oxide layer determines the oxidation rate.

We have selected Computational Materials Science for this work as there have been a number of simulation studies of tungsten oxides published in this journal, including the articles presented below that are cited in this manuscript.

- H. Le, v. Nam, T. Phan, Migrations of oxygen vacancy in tungsten oxide (WO₃): A density functional theory study, Computational Materials Science 90 (2014) 171–176
- W. Liu, P. Jiang, Y. Xiao, J. Liu, A study of the hydrogen adsorption mechanism of W₁₈O₄₉ using first-principles calculations, Computational Materials Science 154 (2018) 53–59.

We have chosen to submit this article to Modelling and Simulation in Materials Science and Engineering, as we believe your readers will be interested in this work.



Thank you for your consideration of this manuscript.

Yours faithfully

Samuel Murphy

2 Munhy 5

Click here to view linked References

Relating the formation energies for oxygen vacancy defects to the structural properties of tungsten oxides

Ryan Kerr^a, Mark R. Gilbert^b, Samuel T. Murphy^{a,*}

^aEngineering Department, Lancaster University, Bailrigg, Lancashire, LA1 4YW, UK ^bUnited Kingdom Atomic Energy Authority, Culham Centre for Fusion Energy, Culham Science Centre, Abingdon, Oxon, OX14 3DB, UK

Abstract

Tungsten is one of the primary materials of choice for several commercial fusion power plant designs, in particular for divertor targets and first wall. In maintenance conditions or during a loss of coolant accident, tungsten is expected to reach temperatures at which it readily volatilises as tungsten trioxide, potentially distributing radioactive material and posing a hazard to personnel. The oxidation of tungsten is reported to show an orientation dependence, however, the mechanism by which it occurs is not fully understood on an atomic level, providing a barrier to the understanding of tungsten smart alloys, which are being developed to reduce oxidation and mitigate the hazards. From the DFT+U simulations, we show how key features of the electronic structure of the tungsten-oxygen system change as the tungsten-oxygen ratio evolves. We then calculate the formation energies of oxygen vacancies and migration barriers for their diffusion, allowing an assessment of their mobility in the different tungsten oxide phases. Our results provide a new level of understanding of the sub-stoichiometric Magnéli phases that are observed during the oxidation of tungsten, which are perceived to be composed of WO₂- and WO₃-like regions.

Keywords: tungsten, WO₃, DFT, vacancy

Email address: samuel.murphy@lancaster.ac.uk (Samuel T. Murphy)

 $^{^* \\} Corresponding \ author$

1. Introduction

Tungsten is a candidate material for use in the first wall and divertor targets of several proposed tokamak fusion devices, including the United Kingdom's STEP project, owing to its favourable thermal and physical properties [1]. However, theoretical studies have shown that pure tungsten first walls may reach temperatures of over 1300 K in the event of a loss of coolant accident [2]. The primary cause of this temperature rise is the decay heat produced by activated tungsten and its decay products, particularly the decay of ¹⁸⁷W, formed via neutron capture by ¹⁸⁶W[3]. At these temperatures, tungsten is known to readily oxidise in the presence of air to form tungsten trioxide, WO₃, which begins at temperatures of around 1000 K[4]. The rapid oxidation of irradiated tungsten enables the mobilisation of both tritium and the activation products of tungsten due to surface volatilisation, posing a safety hazard to first-responders and other on-site personnel[2]. Similar conditions may be encountered during maintenance activities and decommissioning, thereby requiring strict atmospheric control. Alternatively, a deeper understanding of how and why tungsten oxides form is key to guiding materials choices and the development of new, radiationand oxidation-resistant materials for use in future reactor designs.

The oxidation of tungsten has been widely studied over recent decades, but no firm consensus exists as to the mechanism by which it is oxidised to tungsten trioxide, WO₃. It is known to exhibit a strong dependence on oxidation conditions and grain orientation, and to proceed through a series of tungsten oxides as oxygen content in the system increases.[5] This process is well-summarised in the work of Cifuentes et al.: at around 600 °C, $W_{18}O_{49}$ (WO_{2.72}) forms a protective oxide-metal interface, which cracks as it reaches a critical thickness. Subsequent ingress of oxygen through these cracks leads to the formation of columnar $W_{25}O_{73}$ (WO_{2.92}), leading to rapid growth of the oxide scale, followed by eventual transformation into WO₃ as the oxygen concentration at the interface grows[6]. Under the Wagner theory of oxidation, the growth of the oxide layer is controlled by the rate of ion transport and is dependent on the

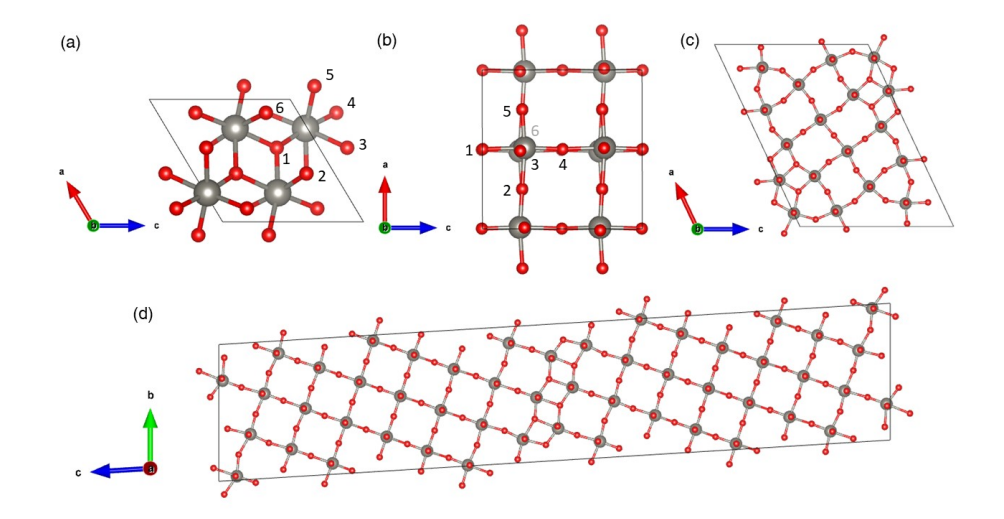


Figure 1: Crystal structures of (a) WO_2 , (b) WO_3 , (c) $W_{18}O_{49}$ ($WO_{2.72}$) and (d) $W_{25}O_{73}$ ($WO_{2.92}$). Grey atoms denote tungsten. Red atoms denote oxygen. Oxygen sites in WO_2 and WO_3 are denoted by the numbers 1 through 6.

concentration gradients through the oxide scale[7]. As such, in this work, we consider the role of oxygen vacancies as the means of establishing a concentration gradient in the oxide phases of interest, which are discussed below.

1.1. Crystallography

This brief summary highlights the key tungsten oxide phases. A description of each is provided below and illustrations are presented in Figure 1:

- a) Tungsten trioxide exhibits a range of polymorphs in the temperature range of 0 < T < 1000 K: monoclinic, < 223 K; triclinic, 223 288 K; monoclinic, 288 603 K; orthorhombic, 603 1013 K; tetragonal, > 1013 K. The room temperature monoclinic phase with the space group $P2_1/c$ is studied in this work. This phase includes three unique oxygen sites at the 4e Wyckoff positions, each bonded to two equivalent W^{6+} ions also at 4e Wyckoff positions [8, 9].
- b) Tungsten dioxide, WO2, which is observed at lower temperatures and

- oxygen partial pressures. The most stable phase of WO₂ crystallises in the monoclinic $P2_1/c$ space group. One W⁴⁺ ion occupies one 4e Wyckoff position, whilst two inequivalent oxygen ions occupy 4e Wyckoff positions [10, 11, 12].
 - c) The W₁₈O₄₉ phase (alternatively WO_{2.72}), which exhibits a tungsten bronze-like structure in the monoclinic P2/m space group, with a β angle of 115.20°according to Salje et al. This phase consists of 16 oxygen ions at 2n Wyckoff positions, 9 at 2m Wyckoff positions, and 1 oxygen ion at the 1f Wyckoff position. The tungsten ions, in a 10:8 mixture of W⁵⁺ and W⁶⁺ oxidation states, occupy the 2n Wyckoff positions[13, 14].
- d) The W₂₅O₇₃ phase (alternatively WO_{2.92}), which exhibits a sheer structure of the monoclinic P2/c space group with a β angle of 98.3°. This phase consists of 37 unique oxygen sites, 1 at the 2f Wyckoff positions and the remaining at the 4g Wyckoff positions. The tungsten ions occupy 13 unique sites, one at the 2f Wyckoff position and the remainder at the 4g Wyckoff positions, in a 1:12 mixture of W⁵⁺ and W⁶⁺ oxidation states[15].

In this work, we examine the thermodynamics and kinetics for oxygen transport, mediated via vacancies, through the tungsten oxide phases WO_2 , WO_3 , and the so-called 'Magnéli' phases $W_{18}O_{49}$ and $W_{25}O_{73}$ to better understand the oxidation process. To support our discussion we provide a detailed review of the physical structure of each phase and investigation into the evolution of their electronic structures with increasing oxygen content.

2. Methodology

2.1. Density Functional Theory

All calculations herein were performed at the DFT level of theory as implemented in the VASP package[16, 17, 18, 19]. Standard PAW pseudopotentials

were used with 14 valence electrons for W, treating the 5s, 6s, 5p and 5d electrons as valence, and 6 valence electrons for O, treating the 2s and 2p orbitals as valence. A plane-wave cut-off energy of 520 eV was selected and a Monkhorst-Pack k-point mesh was optimised for each structure. In all cases the k-point grids were converged to ensure a tolerance of 1 meV per atom. For unit cells, the dimensions of the Monkhorst-Pack grids were: WO₃, $6 \times 6 \times 6$; WO₂, $8 \times 8 \times 8$; W₁₈O₄₉, $1 \times 4 \times 1$; W₂₅O₇₃, $6 \times 1 \times 1$. Gaussian smearing with a smearing width of 0.2 eV was applied to the electronic bands. In ionic relaxation, the ionic positions, cell volume and shape were relaxed until the maximum force exerted on any atom in a single dimension met the criterion |F| < 1 meV/Å. All calculations were performed spin-polarised and the magnetic moments were allowed to relax to their ground state configurations.

In order to account for on-site Coulombic interactions between localised W 5d electrons, all calculations have been performed under the rotationally invariant DFT+U formalism as described by Dudarev et al., i.e., $U_{eff} = U - J$ [20]. In this work, J = 0, and hence $U_{eff} = U$, which has been calculated ab initio under the linear response ansatz described by Cococionni et al. [21]. For a singular W atom, a small change is made in the U parameter, V, ranging from V = -0.25 eV to 0.25 eV in steps of 0.05 eV. At each step, the occupancy of the W 5d orbitals of the atom is computed in both the self-consistent and non-self-consistent fields. The W 5d occupancies are then plotted against V, and the U parameter is calculated as:

$$U = \chi^{-1} - \chi_0^{-1} \approx \left(\frac{\partial N_I^{SCF}}{\partial V_I}\right) - \left(\frac{\partial N_I^{NSCF}}{\partial V_I}\right)^{-1} \tag{1}$$

where, N_I^{SCF} and N_I^{NSCF} is the number of electrons occupying the d orbital of the W atom to which V is applied in the self-consistent field and non-self-consistent field settings respectively. As such, the U parameters used in this work are: WO₃, 5.13 eV; WO₂, 4.84 eV; W₁₈O₄₉, 4.23 eV; W₂₅O₇₃, 3.75 eV.

2.2. Defect Formalism

The formation energy of the oxygen vacancies in the tungsten oxide phases
has been calculated according to equation 2:

$$\Delta E_f^i = E_{\text{defect}} - E_{\text{perfect}} + \mu_O + q(E_{\text{VBM}} + \varepsilon_f) + E_{\text{corr}}$$
 (2)

where, $E_{\rm perfect}$ is the DFT energy of the perfect system, $E_{\rm defect}$ is the DFT energy of the system with one oxygen vacancy, μ_O is the chemical potential of oxygen, q is the charge of the vacancy (in non-metallic systems), $E_{\rm VBM}$ and ε_f are the energies of the valance band maximum and Fermi level respectively, and $E_{\rm corr}$ is the Kumagai charge correction term to account for the finite size of the simulation supercell[22]. The dielectric tensor for WO₃ has been calculated ab initio, using density functional perturbation theory (DFPT) as implemented in VASP. The calculated tensor is predicted to be roughly isotropic:

$$\epsilon = \begin{bmatrix} 57.02 & 0.01 & -0.07 \\ -1.02 & 58.06 & -1.02 \\ -0.07 & 0.01 & 54.77 \end{bmatrix}$$
 (3)

Calculation of defect formation energies was performed in supercells, however, the exact size of the supercell depended on the system of interest. For WO₃ and WO₂ supercells were constructed from $3\times3\times3$ replications of unit cells, whilst for W₁₈O₄₉ and W₂₅O₇₃ supercells were constructed from $1\times2\times1$ repetitions of the unit cells. During optimisation of the defect-containing supercells, the lattice parameters remained fixed to best mimic an isolated defect. While for the examination of the crystal structures we present results using a range of functionals, only the Generalised Gradient Approximation functional of Perdew *et al.* is used for the defect simulations.

The chemical potential of oxygen was defined at two limits. Under the oxygen rich condition, μ_O^{O-rich} was determined from a DFT simulation of the oxygen dimer in an arbitrarily large (a = b = c = 10 Å) unit cell, whose dimensions were constrained during the calculation. The O-O bond length was then optimised and the energy of the system extracted and halved to find μ_O =

-4.94 eV with a bond length of 1.211 Å (compared to 1.207 Å experimentally). In the oxygen poor limit the chemical potential was determined according to:

$$\mu_O^{O-poor} = \mu_{WO_x} - \mu_{W_{(s)}} \tag{4}$$

where, μ_{WO_2} and $\mu_{W_{(s)}}$ are the chemical potentials of the tungsten oxide and tungsten metal respectively. The chemical potential of W was taken as the DFT energy of a single atom in bcc W, $\mu_{W_{(s)}} = -12.98$ eV.

2.3. Activation Energies

Activation barriers to diffusion have been calculated using the climbing image nudged elastic band code provided by the VASP Transition State Tools package[23]. In the case of WO₃ we calculate the migration energy for the +2, +1 and 0 charge states.

3. Results and Discussion

3.1. Crystal Structure

For each phase of interest, the lattice parameters, cell angles and band gaps calculated using different exchange correlation functionals are presented in Table 1. Local and semi-local exchange-correlation functionals, such as the Local Density Approximation (LDA) and the Generalized Gradient Approximation (GGA) functionals, are known to underestimate the band gap, E_g , while hybrid functionals such as HSE06 are expected to give much more accurate values[30]. However, the use of hybrid functionals is prohibitively costly for studying the large number of defect formation energies required in this work. Further, there are known issues with the application of hybrid functionals to metallic materials[31]. Therefore, in this work, the HSE06 functional is only used to calculate the band gap in WO₃.

For room-temperature monoclinic WO₃, the results presented in Table 1 show that DFT overestimates the lattice parameter, irrespective of the functional used. This trend is particularly marked for the semi-local functionals.

however, is still evident when the hybrid HSE06 functional is employed. Although there is some deviation in the lattice parameters calculated in this work compared to the experimentally observed values, the values presented in this work agree with previous DFT studies[25, 24].

Upon examination of individual W-O bond lengths within one WO₆ octahedra, it is seen that the average bond length in WO₃ is around 1.94 Å when optimised using the PBE exchange-correlation functional. As shown in Table 3, there is a considerable distortion in the a-axis when optimised using the PBE functional. The deviation in our calculated structural parameters may be due to the initial structure employed in these calculations, which were available on the Inorganic Crystal Structural Database. There is a degree of uncertainty in the positions of oxygen ions introduced by the Rietveld refinement of neutron powder refraction and X-ray diffraction experiments[32, 33, 34]. Combined with the close similarities in structure between the various tungsten trioxide phases, there is an increased likelihood of the structure relaxing into a local DFT minima.

A similar discrepancy versus experimental data is observed in monoclinic WO₂ using the PBE functional, particularly in the a- and c-axes. However, our results are in line with previous DFT studies on the same phase. In addition, the average bond length in WO₂ optimised using the PBE exchange-correlation functional is 2.08 Å. This is considerably higher than the average bond length in WO₃. However, there is much more distortion in the bond lengths in WO₂ when optimised using the PBE functional compared to the LDA functional.

 $W_{25}O_{73}$ and $W_{18}O_{49}$ were optimised using only the PBE exchange-correlation functional. The lattice parameters obtained for these phases are much closer to the experimentally observed values, although the computed values in the a- and c-axes for $W_{25}O_{73}$ are slightly larger. Upon examination of the structure of $W_{25}O_{73}$, the overestimation of the lattice parameters in the a- and c-axes may be attributed to the similarity in geometry between this phase and WO_3 , as the former contains large regions of corner-sharing WO_6 octahedra whilst the latter consists solely of the same octahedral motifs.

3.2. Electronic Structure

The projected density of states (PDOS) for each phase of interest was obtained using the PBE functional with the DFT+U formalism. Figure 2 shows the gradual evolution of the total density of states with increasing oxygen content, from WO₂ through to WO₃. The PDOS of the W 5d and O 2p states are shown in blue and red respectively, and each plot is shifted such that the Fermi level is at zero. WO₂, W₁₈O₄₉ and W₂₅O₇₃ are all predicted to be metallic, with their Fermi levels lying within bands exhibiting primarily W 5d character. Experimentally, W₁₈O₄₉ is shown to possess semiconductor properties due to its surface being covered with oxygen atoms, however, bulk W₁₈O₄₉ is metallic[35]. In WO₂, there is a band of W 5d states just below the Fermi level; as the oxygen content of the system increases, this band increases in energy and eventually forms the conduction band seen in the DOS of WO₃. The Magnéli phases exhibit features from the DOS of both WO₂ and WO₃, and the band gap exhibited in WO₃ can first be seen in the DOS of W₁₈O₄₉, although the Fermi level is still within the band.

The magnetic moments of each atom in each phase were allowed to relax to their lowest-energy configurations. In WO₂, ferromagnetic ordering was predicted with magnetic moments of approximately $+0.890~\mu_B$ on each W atom. In W₁₈O₄₉, ferromagnetic ordering was predicted with magnetic moments ranging from +0.146 to $+0.494~\mu_B$ on each W atom. The distribution of magnetic moments is shown in Figure 3. In W₂₅O₇₃, a total magnetic moment of $+0.005~\mu_B$ was predicted, indicating negligible magnetic ordering. Finally, in WO₃, the ground state configuration in these calculations was non-magnetic. It is known experimentally that WO₃ is paramagnetic, however, due to the limitations of the software used, the paramagnetic ordering in WO₃ cannot be accurately represented, and therefore the non-magnetic configuration is taken as the best available approximation[13]. Nevertheless, the decreasing magnetic moments between WO₂ and WO₃ is commensurate with magnetic susceptibility experiments performed on these phases[36]. Henceforth, any discussion regarding the perfect crystals of these phases refers to those in their magnetic ground states

described here.

As discussed above, semi-local functionals typically underestimate the band gaps in insulating materials. This is evident in Figure 2 where, for WO₃, the band gaps is shown to be about 1.34 eV. This is almost half of what has been experimental observed, which lies in the range of 2.6 to 2.8 eV. Varying the U parameter between U=0 eV and U=6 eV has a marginal effect on the size of the band gap in WO₃, as shown in Figure 4; an increase in the U parameter from 0 to 5.13 eV raised the band gap by approximately 0.2 eV. However, using the hybrid HSE06 functional, the band gap is predicted to be $E_g=2.53$ eV, which closely matches previous hybrid DFT studies on WO₃ (2.56 eV)[24].

3.3. Oxygen vacancy defect formation energies

The oxygen vacancy formation energies for WO₃ as a function of the Fermi level are presented in Figure 6 (note the plot is presented up to the band gap predicted using the HSE06 functional). In each plot, the black line denotes the vacancy formation energy of the $V_{\rm O(1)}$ defect, the blue line the $V_{\rm O(2)}$ and the red line the $V_{\rm O(3)}$ defect. The positions of these defects are shown in Figure 5. The trend observed is similar to that predicted by Linderälv[37]. At the valance band maximum ($E_F = 0$), the oxygen vacancy $V_{\rm O(2)}^{2+}$ defect exhibits the lowest formation energy at each charge state, which corresponds to the oxygen site which lies between the plane of tungsten atoms. At the valence band maximum the formation energy is -0.98 eV in the O-rich limit and -3.29 eV in the O-poor limit. There is a discrepancy between the formation energies for the charged defects and those presented by Linderälv. This can be explained by the difference in the choice of the charge correction and, in particular, the dielectric tensor used in the employed in the correction.

Figure 6 shows that the charge neutral defect is predicted to have the lowest formation energy at the conduction band minimum, and that there is a narrow region in the mid gap (between 1.60 and 1.65 eV) where the $V_{\rm O(2)}^{1+}$ defect is dominant.

WO₂ is metallic, therefore, only the neutral charge state is considered for

the two unique oxygen vacancy sites, labelled 1 and 2 in Figure 5. The values calculated for the oxygen vacancy formation energies in WO₂ are summarised in Table 4, clearly showing the wide range of formation energies and the effect of the chemical potential of oxygen. In the oxygen-poor limit, the values presented here agree with those proposed by Huang $et\ al.\ (2.49\ eV)$, who calculated the chemical potential of oxygen in the manner described here with a U parameter of 6.2 eV [38].

On the other hand, the values presented in this work are considerably higher in the oxygen-rich limit than those proposed by Linderälv (3.54 eV and 2.98 eV respectively). In both this work and the work of Linderälv, the μ_O has been defined as half the energy of an oxygen dimer, and in this work this has been calculated from a DFT simulation on an isolated dimer in a vacuum using the PBE functional. Whilst the exact value of μ_O is not reported in Linderälv's work, the value of μ_O calculated in this work is slightly higher than the experimental value of -5.23 eV, and higher still than previous theoretical values of around -6.00 eV, calculated using GGA functionals[39, 40]. It is known that the overbinding of GGA functionals, especially in O₂, leads to a larger value of μ_O . Wang et al. proposes a correction of -1.36 eV on the energy of the O₂ dimer to compensate for this overbinding[41]. In this work, the suggested correction has not been applied as the chemical potential calculated herein (-4.94 eV) is much closer to the experimental value.

The Magnéli phases $W_{18}O_{49}$ and $W_{25}O_{73}$ are vastly more complicated than those of WO_2 and WO_3 . These phases have 25 and 147 unique oxygen vacancy sites respectively. We present the oxygen vacancy formation energies in the oxygen-rich limit in Figure 7. The highest values of the vacancy formation energies occur in regions of the unit cell which are comprised of WO_2 -like motifs, whereby each oxygen atom is coordinated to three tungsten atoms. Oxygen vacancy formation energies in these regions are as high as 6.57 eV in $W_{18}O_{49}$. On the other hand, the lowest oxygen vacancy formation energy is found in the center of the unit cell, bridging two WO_6 octahedra, with a value of 3.55 eV.

For both $W_{18}O_{49}$ and $W_{25}O_{73}$, in the regions where the oxygen vacancy

formation energy is higher, oxygen is coordinated to three tungsten atoms with a bond length of between 1.98 and 2.09 Å. This is comparable to the W-O bond lengths predicted in WO₂, which are around 2.08 Å. Lower oxygen vacancy formation energies are found in regions where oxygen is coordinated to only two tungsten atoms (as in WO₃), where shorter bond lengths of between 1.84 and 1.97 Å are observed. Again, this is comparable to the W-O bond lengths predicted in WO₃, which are around 1.94 Å. From these observations, the Magnéli phases appear to be composed of WO₃-like and WO₂-like regions, both in terms physical and electronic structure.

3.4. Oxygen Vacancy Migration Barriers

Finally, we present the migration barriers between oxygen vacancy sites in WO₃ and WO₂. The values calculated for the neutral (q=0) system closely correspond to existing data reported by Le *et al.*, who reported migration barriers of ≈ 0.14 eV for the $V_O^{(1)} \longrightarrow V_O^{(2)}$ pathway and values between $0.87 \approx 1.07$ eV for the $V_O^{(1)} \longleftrightarrow V_O^{(3)}$ pathway[42]. Therefore, the accuracy of the one-image NEB calculations employed in this work is considered sufficient.

As shown in Table 5, the migration barrier required to migrate the $V_O^{(1)}$ vacancy to $V_O^{(2)}$ vacancy, and from $V_O^{(3)}$ to $V_O^{(2)}$, is considerably smaller than the energy required to move between vacancies $V_O^{(1)}$ and $V_O^{(3)}$. This corresponds to a preference in oxygen moving along the a-axis. Furthermore, the q=+1 system exhibits noticeably different migration energies to the q=0 and q=+2 systems, likely due to the unpaired electron present in this system. The anisotropy in the migration energies suggests that the orientation of WO₃ may impact the rate at which the oxide interface grows into tungsten, aligning with the orientation dependency observed by Schlueter $et\ al.[5]$.

In WO₂, the migration barrier of oxygen diffusion is strongly directional. The migration barrier required to migrate the $V_O^{(1)}$ vacancy to the $V_O^{(2)}$ vacancy is 1.81 eV, whilst migration in the reverse direction has an migration barrier of 2.90 eV. Similar values were obtained by Huang *et al.*, in which the migration barriers for the migrations described above were 1.86 eV and 2.19 eV respectively[38].

The significantly larger migration barriers means that WO₂ is far less permeable to oxygen compared to WO₃, indicating that WO₂ and WO₂-like regions in the Magnéli phases protect the pure tungsten metal from further oxidation. This protective behaviour has been observed experimentally and attributed broadly, but not unanimously, to WO₂ or the Magnéli phases[6, 43, 44].

4. Conclusion

In this work, we have reviewed the physical structure of the key tungsten oxide phases observed during the oxidation of tungsten. As the tungsten-oxygen ratio evolves, from WO_2 through to WO_3 , we see a corresponding evolution of the electronic density of states for each phase. The W 5d states which lie just below the Fermi level in WO_2 shift to higher energies as the oxygen content increases, until they rise above the Fermi level in WO_3 , which becomes an insulator.

By investigating the evolution of the electronic structure, the bond lengths in the WO₂ and WO₃ phases, and the oxygen vacancy formation energies of the four tungsten-oxygen systems of interest, we show that the substoichiometric phases, W₁₈O₄₉ and W₂₅O₇₃, can be considered to be made of regions displaying WO₂-like and WO₃-like properties (namely, bond lengths and oxygen vacancy formation energies). It is suggested that the oxygen diffusion migration barriers may exhibit similar trends. This would account for the orientation dependence of the oxidation of tungsten, as well as the observation that the Magnéli phases only form thin, transient layers between WO₂ and WO₃. It has been shown that the migration barriers of oxidation diffusion in WO₂ are much larger than those observed in WO₃ (1.81 \sim 2.90 eV vs. 0.15 \sim 0.80 eV respectively). Furthermore, it is shown that oxygen migration in the $\langle 100 \rangle$ direction is strongly preferred in WO_3 , with migration barriers as little as 0.13 eV in the +2 charge state. Therefore, if the Magnéli phases are orientated such that their a-axis lies perpendicular to the oxide-air interface, rapid diffusion of oxygen would be expected through through the WO₃-like regions. However, should they be orientated such that their WO₂-like regions occlude the WO₃-like regions from the oxide-air interface, then diffusion of oxygen through the b- or c-axes would be much slower. In this way, the orientation dependence of the system and the effect of the formation of columnar W₂₅O₇₃ on the oxidation of tungsten arises out of the oxygen vacancy formation energies and diffusion barriers.

5. Acknowledgements

Via our membership of the UK's HEC Materials Chemistry Consortium, which is funded by EPSRC (EP/R029431), this work used the ARCHER2 UK National Supercomputing Service (http://www.archer2.ac.uk). This work was also part-funded by the EPSRC Energy Programme (grant number EP/W006839/1). We wish to acknowledge the use of the EPSRC funded Physical Sciences Datascience Service hosted by the University of Southampton and STFC under grant number EP/S020357/1. This work was also supported by the ESPRC-funded Centre for Doctoral Training in GREEN (Growing skills for Reliable Economic Energy from Nuclear) (Grant code: EP/S022295/1).

References

- [1] D. Stork, et al., Materials R&D for a timely DEMO: Key findings and recommendations of the eu roadmap materials assessment group, Fusion Engineering and Design 89 (7) (2014) 1586–1594.
- [2] D. Adomavicius, M. Lisak, A conceptual study of commercial fusion power plants, EFDA RP RE 5.0, 2005.
 - [3] Decay heat experiment featuring low-energy neutron induced tungsten-187 production in iter baffle plates and its analysis, Fusion Engineering and Design 51-52 (2000) 809–814.
- [4] M. Togaru, et al., Direct observation of tungsten oxidation studied by in situ environmental TEM, Materials Characterization 174 (2021) 111016.

- [5] K. Schlueter, M. Balden, Dependence of oxidation on the surface orientation of tungsten grains, International Journal of Refractory Metals and Hard Materials 79 (2019) 102–107.
- [6] S. Cifuentes, M. Monge, P. Pérez, On the oxidation mechanism of pure tungsten in the temperature range 600–800°C, Corrosion Science 57 (2012) 114–121.
 - [7] A. Atkinson, Wagner theory and short circuit diffusion, Materials Science and Technology 4 (12) (1988) 1046–1051.
- [8] E. Indrea, E. Bica, E.-J. Popovici, R.-C. Suciu, M.-C. Rosu, D. Silipas, Rietveld refinement of powder x-ray diffraction of nanocrystalline noble metals tungsten trioxide, Revue Roumaine de Chimie 56 (2011) 589–593.
 - [9] T. Vogt, P. M. Woodward, B. A. Hunter, The high-temperature phases of WO₃, Journal of Solid State Chemistry 144 (1) (1999) 209–215.
- [10] V. L. Shaposhnikov, D. B. Migas, V. N. Rodin, V. E. Borisenko, Ab initio investigation of structural and electronic properties of tungsten dioxide, Physica Status Solidi (b) 248 (6) (2011) 1471–1476.
 - [11] R. Diehl, G. Brandt, E. Saije, The crystal structure of triclinic WO_3 , Acta Crystallographica Section B 34 (4) (1978) 1105–1111.
- 375 [12] W. L. Kehl, R. G. Hay, D. Wahl, The structure of tetragonal tungsten trioxide, Journal of Applied Physics 23 (2) (1952) 212–215.
 - [13] E. Salje, The orthorhombic phase of WO₃, Acta Crystallographica Section B 33 (2) (1977) 574–577.
- [14] K. Viswanathan, K. Brandt, E. Salje, Crystal structure and charge carrier
 concentration of W₁₈O₄₉, Journal of Solid State Chemistry 36 (1) (1981)
 45–51.

- [15] M. Sundberg, The crystal and defect structures of W₂₅O₇₃, a member of the homologous series W_nO_{3n-2}, Acta Crystallographica Section B 32 (7) (1976) 2144–2149.
- [16] G. Kresse, J. Hafner, Ab initio molecular dynamics for liquid metals, Physical Review B 47 (1993) 558–561.
 - [17] G. Kresse, J. Furthmüller, Efficiency of ab-initio total energy calculations for metals and semiconductors using a plane-wave basis set, Computational Materials Science 6 (1) (1996) 15–50.
- ³⁹⁰ [18] G. Kresse, J. Furthmüller, Efficient iterative schemes for ab initio totalenergy calculations using a plane-wave basis set, Physical Review B 54 (1996) 11169–11186.
 - [19] G. Kresse, D. Joubert, From ultrasoft pseudopotentials to the projector augmented-wave method, Physical Review B 59 (1999) 1758–1775.
- [20] S. L. Dudarev, G. A. Botton, S. Y. Savrasov, C. J. Humphreys, A. P. Sutton, Electron-energy-loss spectra and the structural stability of nickel oxide: An LSDA + U study, Physical Review B 57 (1998) 1505–1509.
 - [21] M. Cococcioni, S. de Gironcoli, Linear response approach to the calculation of the effective interaction parameters in the LDA + U method, Physical Review B 71 (2005) 035105.
 - [22] Y. Kumagai, F. Oba, Electrostatics-based finite-size corrections for first-principles point defect calculations, Physical Review B 89 (2014) 195205.
 - [23] B. Uberuaga, H. Jonsson, A climbing image nudged elastic band method for finding saddle points and minimum energy paths, J. Chem. Phys. 113 (2000) 9901–9904.
 - [24] W. Wang, A. Janotti, C. G. Van de Walle, Role of oxygen vacancies in crystalline WO₃, J. Mater. Chem. C 4 (2016) 6641–6648.

- [25] A. Jain, et al., Commentary: The materials project: A materials genome approach to accelerating materials innovation, APL Materials 1 (1) (2013) 011002.
- [26] S. Tanisaki, Crystal structure of monoclinic tungsten trioxide at room temperature, Journal of the Physical Society of Japan 15 (1960) 573–581.
- [27] R. J. Sáenz-Hernández, et al., Correlation between thickness and optical properties in nanocrystalline γ -monoclinic WO₃ thin films, Coatings 12 (11).
- [28] B. O. Loopstra, H. M. Rietveld, Further refinement of the structure of WO₃, Acta Crystallographica Section B 25 (7) (1969) 1420–1421.
- [29] A. A. Bolzan, B. J. Kennedy, C. J. Howard, Neutron powder diffraction study of molybdenum and tungsten dioxides, Australian Journal of Chemistry 48 (1995) 1473–1477.
- [30] H. Xiao, J. Tahir-Kheli, W. A. Goddard III, Accurate band gaps for semiconductors from density functional theory, The Journal of Physical Chemistry Letters 2 (3) (2011) 212–217.
- [31] J. Paier, M. Marsman, G. Kresse, Why does the B3LYP hybrid functionalfail for metals?, The Journal of Chemical Physics 127 (2) (2007) 024103.
 - [32] A. A. Yaremchenko, D. D. Khalyavin, M. V. Patrakeev, Uncertainty of oxygen content in highly nonstoichiometric oxides from neutron diffraction data: example of perovskite-type Ba_{0.5}Sr_{0.5}Co_{0.8}Fe_{0.2}O₃, J. Mater. Chem. A 5 (2017) 3456–3463.
- ⁴³⁰ [33] J. A. Kaduk, Chemical reasonableness in rietveld analysis: Inorganics, Powder Diffraction 22 (3) (2007) 268–278.
 - [34] B. S. J, P. Tian, Testing different methods for estimating uncertainties on rietveld refined parameters using sr rietveld 226 (12).

- [35] W. Liu, P. Jiang, Y. Xiao, J. Liu, A study of the hydrogen adsorption mechanism of $W_{18}O_{49}$ using first-principles calculations, Computational Materials Science 154 (2018) 53–59.
 - [36] M. J. Sienko, B. Banerjee, Studies in non-stoichiometry: Magnetic susceptibilities in the tungsten-oxygen system1, Journal of the American Chemical Society 83 (20) (1961) 4149–4152.
- 440 [37] C. Linderälv, Structural and thermodynamical properties of tungsten oxides from first-principles calculations, Chalmers University of Technology (2016).
 - [38] S. Huang, R. Kerr, S. Murphy, M. R. Gilbert, J. Marian, Multilayer interface tracking model of pure tungsten oxidation, Modelling and Simulation in Materials Science and Engineering 30 (8) (2022) 085015.
 - [39] B. He, H. Zhou, F. Yang, W.-K. Li, A method for calculating the heats of formation of medium-sized and large-sized molecules, Open Journal of Physical Chemistry 05 (03) (2015) 71–86.
- [40] B. Hammer, L. B. Hansen, J. K. Nørskov, Improved adsorption energetics within density-functional theory using revised perdew-burke-ernzerhof functionals, Physical Review B 59 (1999) 7413–7421.
 - [41] L. Wang, T. Maxisch, G. Ceder, Oxidation energies of transition metal oxides within the GGA+U framework, Physical Review B 73 (2006) 195107.
- [42] H. Le, v. Nam, T. Phan, Migrations of oxygen vacancy in tungsten ox ide (WO₃): A density functional theory study, Computational Materials
 Science 90 (2014) 171–176.
 - [43] E. A. Kellett, S. E. Rogers, The structure of oxide layers on tungsten, Journal of The Electrochemical Society 110 (6) (1963) 502.
- [44] J. Habainy, S. Iyengar, K. B. Surreddi, Y. Lee, Y. Dai, Formation of oxide layers on tungsten at low oxygen partial pressures, Journal of Nuclear Materials 506 (2018) 26–34.

Lattice Parameters / Å Vol /ų E_g/eV XC Functional U /eV b $\beta/^{\circ}$ Ref a \mathbf{c} WO_3 LDA *5.137.61 7.617.63 90.01 441.870.79PBE * 5.137.6890.09 458.307.717.741.34 HSE06 * 0.007.53 7.62 7.69 90.77445.762.53 HSE06 0.007.39 7.647.75 90.3 440.432.80 [24]PBE 5.20 7.72459.49 7.687.75 91.50 [25]422.16 Tanisaki et al. 7.30 7.53 7.68 90.54[26] Saenz et al. 7.307.54 7.69 90.91 423.27[27]Loopstra et al. 7.317.547.6990.9 423.85 $2.6 \sim 3.2$ [28] WO_2 LDA *4.84 5.52 4.89152.245.64 120.42 PBE * 165.994.845.61 4.955.72120.93 PBE 0.005.824.965.75120.48 156.44[10] PBE 5.205.624.955.72120.93 159.12[25] Bolzan et al. 5.57 4.90 5.66 120.68 154.48[29] $\mathrm{W}_{18}\mathrm{O}_{49}$ PBE * 4.1318.323.78 14.03971.57115.21PBE 5.20 18.29 3.8614.20 109.71 1008.87 [25]Salje et al. 18.333.79 14.04 115.20 995.41 [14] $\mathrm{W}_{25}\mathrm{O}_{73}$ PBE *3.7512.123.86 59.8393.512799.03 PBE 5.20 12.263.86 60.5797.91 2866.39 [25] 11.93 3.82 59.7298.3 Sundberg et al. 2721.60[15]

Table 1: Lattice parameters and band gaps, E_g , where applicable, for WO₃, WO₂, W₁₈O₄₉ and W₂₅O₇₃. Asterisks (*) denote parameters, cell volumes and band gaps calculated in this work. Experimental values are indicated with a U parameter of '-', whereas DFT studies which have not applied a U parameter are listed as U = 0. Similarly, where a band gap has not been evaluated are marked with a '-'.

Table 2: Optimised bond lengths in WO_3 .

	V	$W - O_x$	Bond	l Leng	th / A	Å
XC Functional	1	2	3	4	5	6
LDA	1.93	1.88	1.90	1.91	1.95	1.86
PBE	1.87	2.00	1.96	1.90	1.85	2.03
HSE06	1.81	2.00	2.01	1.82	1.76	2.16

Table 3: Optimised bond lengths in WO_2 .

	$W-O_x$ Bond Length / Å				Ţ	
XC Functional	1	2	3	4	5	6
LDA	2.06	2.06	2.00	2.00	2.00	1.95
PBE	2.07	2.05	2.09	2.11	2.03	2.01

Table 4: Formation energies of oxygen vacancies in WO_2 under oxygen rich and oxygen poor conditions.

	Formation energy $/$ eV		
Vacancy	O-Rich	O-Poor	
$V_{O(1)}$	5.99	2.54	
$V_{O(2)}$	4.90	1.45	

Table 5: Oxygen vacancy migration barriers through tungsten trioxide in the +0, +1 and +2 charge states between two unique oxygen vacancy sites, i.e., A to B. Values for the reverse migration (B to A) are included in brackets.

Migration barrier / eV

${f q}$	$V_{O(1)} \leftrightarrow V_{O(2)}$	$V_{O(1)} \leftrightarrow V_{O(3)}$	$V_{O(2)} \leftrightarrow V_{O(3)}$
0	$0.153\ (0.733)$	$0.765 \ (0.781)$	$0.799 \ (0.234)$
1	$0.222\ (0.750)$	$0.665 \ (0.664)$	$0.791\ (0.262)$
2	0.126(0.741)	0.726(0.741)	0.780 (0.161)

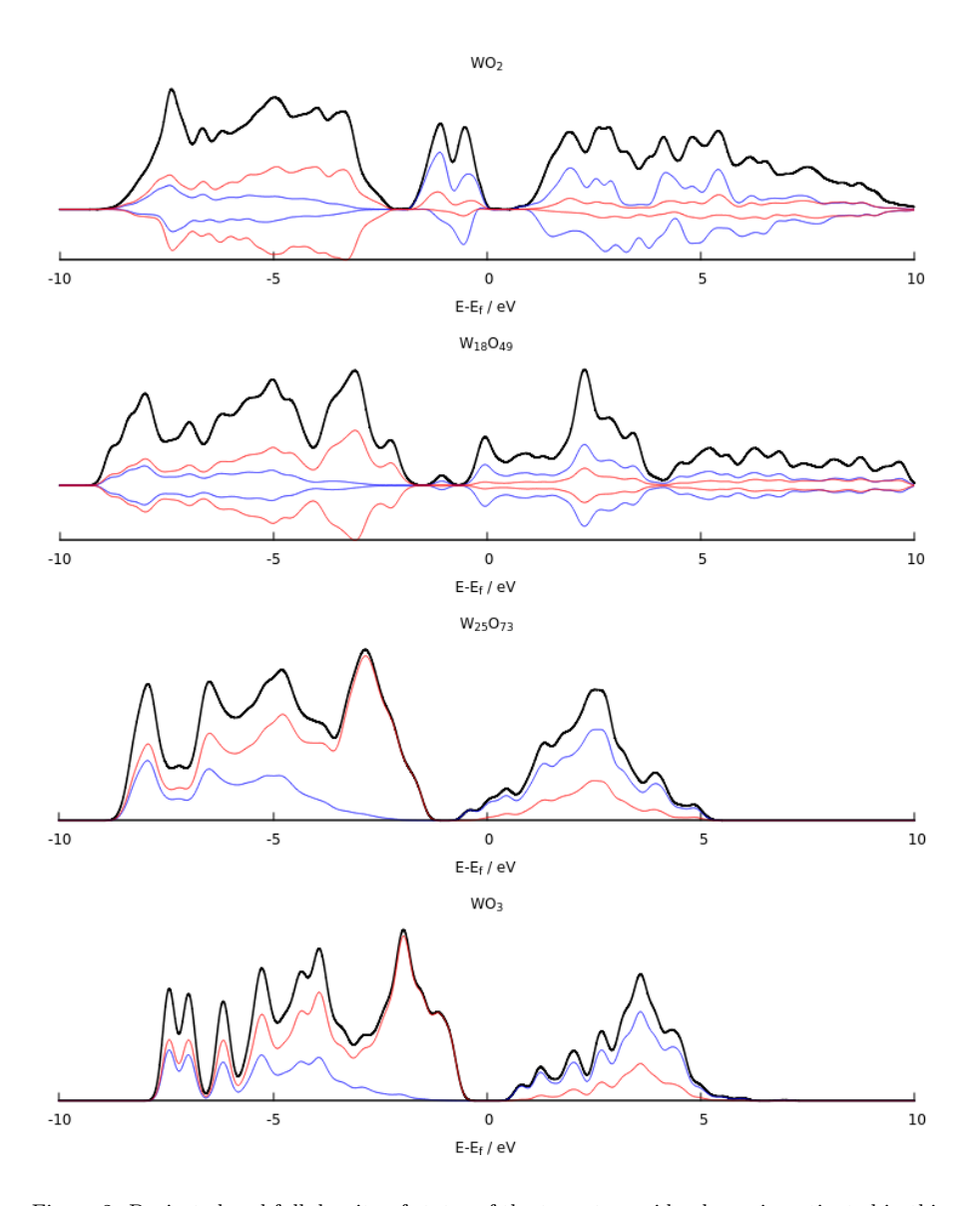


Figure 2: Projected and full density of states of the tungsten oxide phases investigated in this study. The Fermi level has been set to zero.

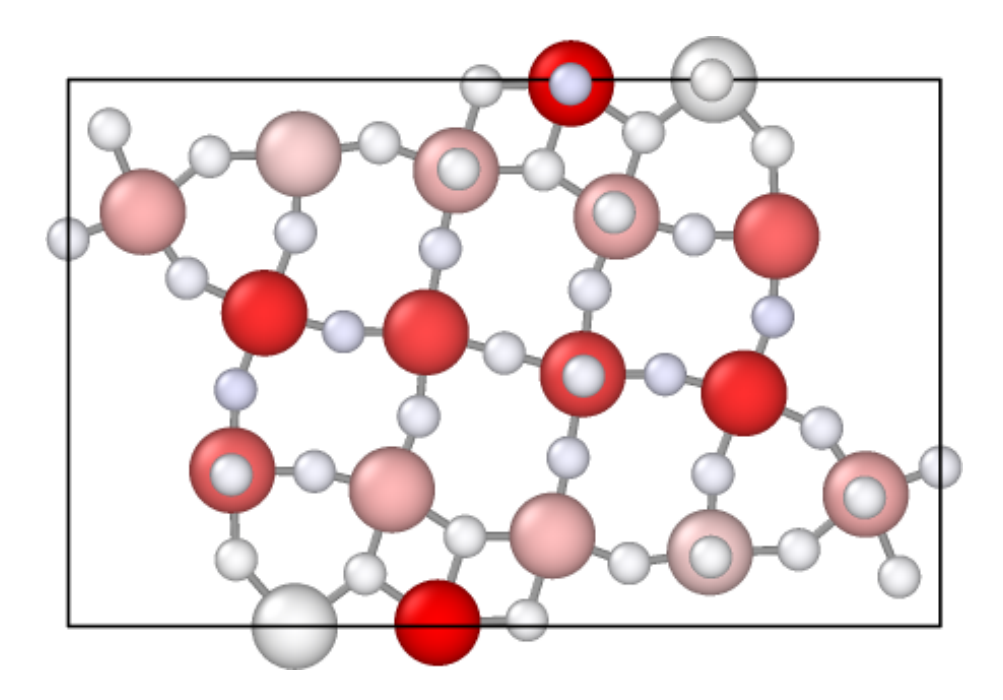


Figure 3: Distribution of magnetic moments in W18O49, ranging from 0.000 μ_B (white) to +0.494 μ_B (red).

Table 6: Oxygen vacancy migration barriers through tungsten dioxide. As there are only two unique oxygen vacancy sites, the migration barrier between two identical, adjacent vacancy sites has also been included.

${\bf Migration~Barrier~/~eV}$

$$\mathbf{q} \quad V_O^{(1)} \leftrightarrow V_O^{(2)} \quad V_O^{(1)} \leftrightarrow V_O^{(1)}$$

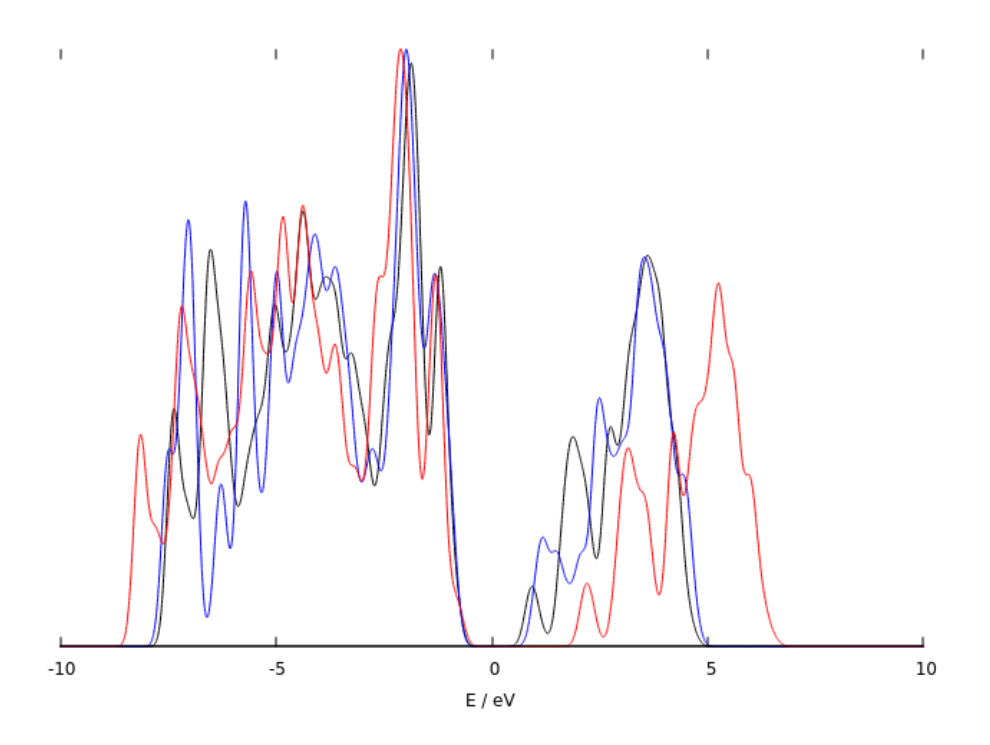


Figure 4: Total density of states for monoclinic WO_3 , calculated with a U parameter of 0 eV (blue line) and 5.13 eV (solid line). The total density of states as calculated using the HSE06 hybrid functional is shown in red.

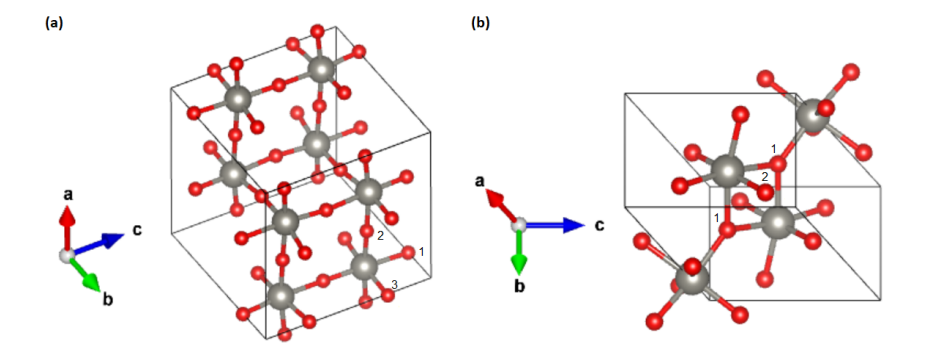


Figure 5: Definitions of the unique oxygen vacancies in (a) tungsten trioxide and (b) tungsten dioxide.

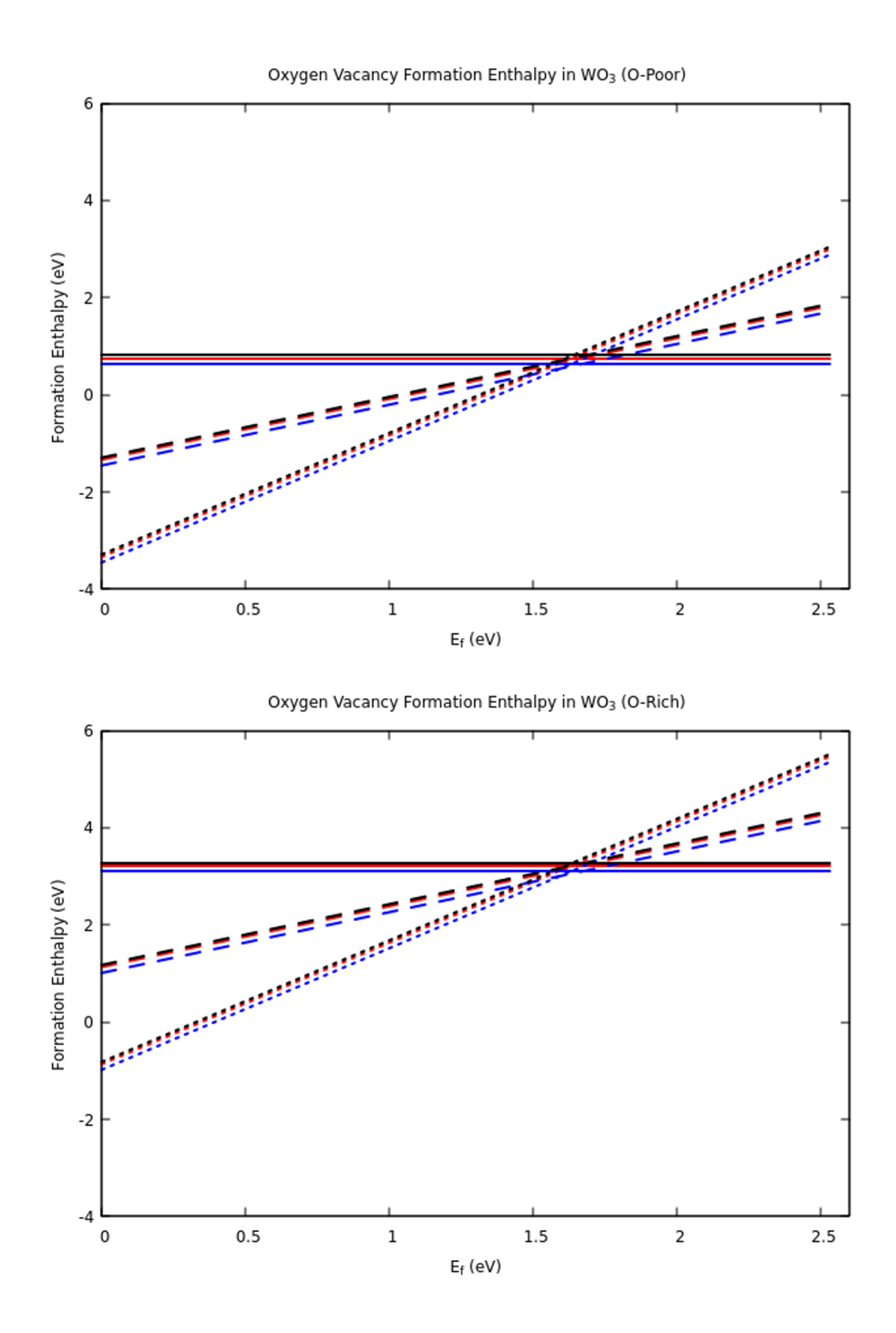
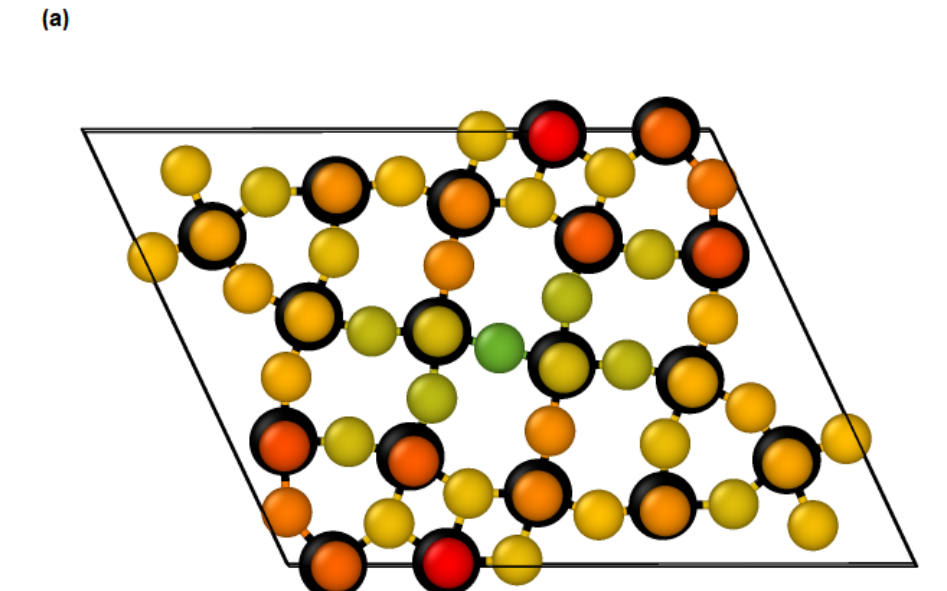


Figure 6: Oxygen vacancy formation energy in tungsten trioxide as a function of the Fermi level in both the O-rich and O-poor limits. The solid line denotes the +0 charge state, the dashed line denotes the +1 charge state, and the dotted line denotes the +2 charge state. The valence band maximum lies at 0 eV, whilst the conduction band maximum begins at 2.53 eV.



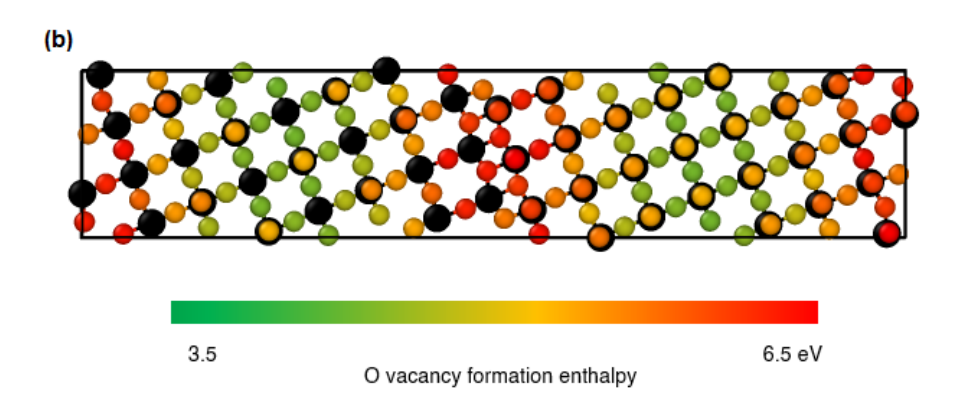


Figure 7: Oxygen vacancy formation energies in the Magnéli phases (a) $W_{18}O_{49}$ and (b) $W_{25}O_{73}$. W ions in black.

Declaration of interests

that could have appeared to influence the work reported in this paper.
☐The authors declare the following financial interests/personal relationships which may be considered
as potential competing interests:

⊠The authors declare that they have no known competing financial interests or personal relationships